Applied Materials Today 37 (2024) 102148

Contents lists available at ScienceDirect

Applied Materials Today

journal homepage: www.elsevier.com/locate/apmt

Towards a self-healing aluminum metal matrix composite: Design, fabrication, and demonstration

David Svetlizky [a], Baolong Zheng [b], Xin Wang [b], Sen Jiang [b], Lorenzo Valdevit [b], Julie M. Schoenung [b,c], Enrique J. Lavernia [b,c], Noam Eliaz [a,*]

[a] Department of Materials Science and Engineering, Tel-Aviv University, Ramat Aviv, Tel Aviv 6997801, Israel
[b] Department of Materials Science and Engineering, University of California Irvine, Irvine, CA 92697-2575, USA
[c] Materials Science & Engineering and Mechanical Engineering, Texas A&M University, College Station, TX 77843-3003, USA

ARTICLE INFO

Keywords:
Aluminum metal matrix composite
Core/shell powder
Self-healing metal-matrix composites (SHMMCs)
Spark plasma sintering (SPS)
Transient liquid phase bonding (TLPB)

ABSTRACT

This paper presents a novel approach to designing and synthesizing a self-healing aluminum-based metal matrix composite (MMC) at the macro-scale. The composite comprises an Al 5083 matrix embedded with low melting point particles (LMPPs) that act as healing agents. A two-step electroless micro-encapsulation process is developed to create LMMPs with a diffusion and thermal barrier designed to protect the Zn-8Al core with a Co-P shell. The MMC is fabricated using spark plasma sintering. Following controlled total fracture under tension, external compressive force is applied during heat treatment to heal the fracture effectively. The evolution of phases and interfaces is characterized using electron microscopy, and transient liquid phase bonding (TLPB) is identified as the fracture-healing mechanism, facilitated in areas with sufficiently high Zn concentration to fill the crack. The design can be expanded to incorporate other matrix and LMMP materials, mechanical crack volume reduction by integrating shape memory alloy (SMA) reinforcement during MMC synthesis, and processing of the self-healing MMC using Directed Energy Deposition additive manufacturing.

1. Introduction

Most metallic structural materials are prone to degradation via irreversible mechanisms such as fatigue, creep, wear, corrosion, etc. All of these limit the service lifetime of structural components and might lead to catastrophic failure. The concept of metal-based self-healing materials (SHMs) has attracted growing interest in recent years in various industries, including the aircraft, automotive, marine, oil, and gas industries [1,2]. Yet, it is in its infancy [3]. Like polymer-based SHMs, metal-based SHMs are inspired by biological systems that can heal damage and recover functionality [4]. However, healing damage in metallic structural parts is much more challenging due to their high melting temperatures, low diffusion rates, oxidation, and complex fabrication [3,4].

Recently, there has been a growing interest in bio-inspired self-healing metal matrix composites (SHMMCs). Currently, three design approaches exist for SHMMCs that enable the repair of cracks at the macro-scale [5]. The first approach involves forming precipitates in oversaturated but under-aged solid solutions. Precipitates preferentially form at voids and cracks, sealing them and slowing their growth. However, this method is limited to ageable alloys and requires long time for recovery. The second approach is reinforcing the alloy matrix with shape-memory alloy (SMA) wires, such as Nitinol (NiTi). When heated above the SMA's austenitic transformation temperature, intrinsic compressive stress is established by the embedded SMA wires, due to the shape memory effect (SME), thus closing the crack mechanically. This approach has limitations in terms of crack orientation, the potential for dramatic changes in MMC properties compared to the matrix material, and inefficiency in high-strength matrices. The third approach embeds a healing agent within the matrix, typically low-melting-point particles (LMPPs). This approach has shown promising results, with the LMPPs filling the crack and facilitating healing [3,5,6]. When the MMC is subject to a temperature above the melting point of the healing agent, but below the melting point of the matrix, the LMP agent flows under capillary action to seal the crack. The LMP agent should sufficiently wet the crack surface and chemically react with the metallic matrix for efficient crack healing. A major challenge with this approach is the need to encapsulate the healing agent in spherical shells, to prevent it from

* Corresponding author.
E-mail address: neliaz@tauex.tau.ac.il (N. Eliaz).

https://doi.org/10.1016/j.apmt.2024.102148
Received 9 November 2023; Received in revised form 15 February 2024; Accepted 28 February 2024

reacting with the matrix during the MMC fabrication, which might result in the formation of undesired phases and properties. The shell should act as an efficient diffusion barrier, but it also fractures easily when a propagating crack crosses it. Another challenge is maintaining the material's structural integrity during healing [5]. Several healing agents have been explored, including Sn–40 Pb [7–9] and Sn–Bi [5,10,11].

SHMMCs can work where a crack location is difficult to reach or common repair techniques are not applicable [12], and hold great potential to increase product lifetime and reliability, increase safety, reduce labor and material costs, and help reduce industry-related global emissions of greenhouse gases. Aluminum-based SHMMCs, in particular, are of great interest in applications such as aircraft structural components, spacecraft structural components for longer missions where current repair technologies like welding and bonding are not an option, and oil-well casings [12].

Files, Manuel et al. [13–19] were the first to investigate SMA-reinforced MMC design concept. The group demonstrated a proof of concept of the design concept on Sn–13Bi and Mg–5.7Zn–2.7Al (at%) matrices reinforced with 1 vol% Nitinol SMA wires [13]. In the first system, 94 ± 1 % ultimate tensile strength (UTS) recovery was achieved, but at the cost of a 66 % decrease in ductility. In the second system, only partial crack enclosure was achieved. Even an increase of the SMA wires content to 30 vol% did not provide sufficient stress to clamp the crack surfaces and did not show adequate ability to facilitate TLP healing of the crack. In another study, Ferguson et al. [20] studied the healing of a matrix made of commercial zinc alloy, ZA–8 (Zn–8Al, wt%), reinforced with NiTi SMA wire. Up to 30 % of the original UTS and ductility were recovered by thermal healing treatment of the ZA–8/SMA MMC. Poormir et al. [21] utilized the Taguchi method to study the influence of the design factors (number of SMA strips, pre-strain, and applied healing temperature) as a means for material design optimization of Sn–13Bi (wt%) alloy reinforced with NiTi SMA strips fabricated by gravity casting. It was reported that utilizing 2.33 vol% SMA, 6 % pre-strain, and healing treatment at 190 °C yielded the optimal UTS and ductility recovery efficiency.

NASA has developed a "clamp and melt" approach where the SHMMC contains both Nitinol SMA wires (2 vol%) and an off-eutectic Al–3Si (at%) alloy matrix that is cast over the continuous wires. The matrix undergoes partial liquefaction during heat treatment [11,12,19,22]. An average recovery of 91.6 % ultimate tensile strength was achieved after heat treatment at 592°C for 24 h. The advantages of the "clamp and melt" approach are that it enables efficient mechanical properties recovery after healing treatment, and that the healing treatment is not limited to single use. On the other hand, this approach has some significant drawbacks: (1) it is exclusive to off-eutectic alloys; (2) it requires high temperature to partially melt the matrix, which might cause changes in geometrical shape and surface roughness as well as reduction of fatigue resistance; (3) heat treatment might damage the SMA wires and cause substantial grain growth and coarsening of the Al matrix; (4) it is a complex fabrication process with multiple steps; (5) using traditional manufacturing processes, it is challenging to design and fabricate SMA-reinforced structures with isotropic healing properties and complex geometries.

Svetlizky has recently suggested a novel design concept according to which the SHMMC will be processed by directed energy deposition (DED) additive manufacturing (AM), and will combine LMPPs with SMA fibers [23]. DED has matured into a powerful tool for high-throughput design and fabrication of advanced materials, including MMCs and SMAs, often with excellent bonding between multiple materials [24–26]. According to Svetlizky's approach, the healing process is facilitated by an extrinsic two-step heat treatment of the cracked part. The MMC is heated above the SMA's austenite transformation temperature in the first step. This leads to compressive stress by the embedded SMA component, facilitating mechanical crack volume reduction by pulling the crack surfaces together in response to the extrinsic heating (namely, an SME). The second step involves a temperature increase to a preset value (~390 °C for ZA–8), which enables complete liquefaction of the micro-encapsulated LMPPs while maintaining the material structural integrity during the healing. Upon liquefaction, capillary forces drive the LMP agent into the crack, ultimately reacting with the metal matrix to seal the crack. This approach has several key advantages: (1) it can serve as a generic type of self-healing design (i.e., not exclusive to off-eutectic matrices); (2) it facilitates self-healing under significantly lower temperatures (e.g., ~390 °C vs. 592°C), resulting in less degradation of either the Al matrix or the SMA; (3) it allows more isotropic healing (if microcapsules are used instead of hollow tubes); (4) it utilizes AM, thus opening an avenue to cost- and time-efficient design and manufacture, and more complex geometries. However, LMP-assisted SHMMCs still present significant challenges: (1) potentially inadequate mechanical properties recovery; (2) void formation after the healing process [3]; (3) complex LMP micro-encapsulation process [3,20]; (4) lack of perfect metallurgical bonding at the interface due to surface oxidation; and (5) formation of undesired phases (e.g. intermetallics) due to the interaction between the LMP and the matrix.

The processing of an aluminum-based SHMMC according to Svetlizky's concept is challenging and requires careful development of several components: (1) Laser Engineered Net Shaping (LENS®) DED of an Al-based alloy that functions as the matrix of the SHMMC [27–29]. (2) Synthesis by gas atomization (GA) of a pre-alloyed ZA–8 powder feedstock for LENS®, and development of chemical/electrochemical processes for micro-encapsulation of the powder feedstock, in either ceramic (e.g., alumina [30]) or metallic (e.g., Ni/NiP [31]) shells, as physical, diffusion, and thermal barriers. The ZA–8 core powder was selected to demonstrate this self-healing design concept because it has mechanical and physical properties similar the utilized Al 5083-O matrix [30]. The formation of Ni/NiP shells consisted of two steps – cementation and autocatalytic deposition. A similar process is developed in the present work to form a CoP shell on the ZA–8 core. Numerical simulations of heat transfer and phase transformation for a core/shell powder particle floating in the Al-based alloy melt pool (unpublished data) yielded longer residence times of ZnAl/CoP particles than ZnAl/NiP particles. In addition, preliminary LENS® processing of MMCs with ZnAl/CoP gave better results compared to those with ZnAl/NiP. Therefore, only ZnAl/CoP powders are used herein. (3) Processing by spark plasma sintering (SPS) of an MMC with Al 5083 matrix and ZnAl/CoP LMPPs as a first proof-of-concept.

Here, we present the successful synthesis of a CoP-coated ZA-8 powder, which is then dispersed in an Al 5083 matrix using SPS, resulting in full density compaction. This innovative encapsulation technique for LMPPs represents a new methodology for self-healing metal matrix composites (SHMMCs), as opposed to previously reported methods such as using ceramic hollow tubes or hollow capsules filled with solder material. A proof-of-concept demonstration of the ability to heal a fully fractured sample is presented by heat treatment under extrinsic pressure, instead of using intrinsic SMA. The study also includes a detailed microstructural analysis to determine the relevant self-healing mechanism by characterizing phases and interfaces.

2. Results and Discussion

2.1. ZA–8/CoP LMMP micro-encapsulation

Electroless deposition from aqueous solutions on Zn-based powders is exceptionally challenging because of the negative standard potential of Zn, extensive hydrogen evolution, and the non-uniform and porous oxide/hydroxide layer that forms over the core's surface [31]. Svetlizky et al. [31] were the first to develop an effective process for electroless plating on Zn powders. A compact, uniform, and conformal Ni/NiP shell on ZA–8 microparticles was demonstrated, without agglomeration.

We utilized a comparable technique to produce a CoP shell, with Co being the preferred material due to its high melting point (1495°C), commendable mechanical properties at elevated temperatures, and

good oxidation resistance. To avoid the formation of an oxide layer and hydrogen evolution during electrodeposition, we developed a two-step encapsulation process: (i) Co cementation (galvanic displacement) was carried out in an ethanol-based solution, causing the reduction of Co along with oxidation of zinc and aluminum. The resulting primary Co cementation layer catalyzes the electroless deposition reaction without being consumed during the process [32]. (ii) Autocatalytic deposition of CoP followed, where the Co reduction occurred concurrently with the oxidation of the sodium hypophosphite reducing agent [33].

Fig 1a–j shows SEM images and related energy-dispersive X-ray spectroscopy (EDS) elemental maps at the surface and cross-section of Zn–Al particles after the two-step encapsulation process, using the optimized conditions reported in Table 2. This Fig affirms the establishment of conformal, uniform, and compact encapsulation over each LMPP. There is no evidence of significant core dissolution or particle agglomeration, although some core oxidation (the dark gray interface between the core and shell in Fig 1d,e is evident. The elemental maps in Fig 1g,j confirm the co-deposition of Co and P in the outer shell. Fig 1 and **Fig S1** reveal neither cracking nor delamination of the shell on the spherical particles. However, many micro-grooves are evident at the outer surface (Fig 1c), which might make these particles brittle during deformation. The thickness of the shell was controlled by applying multiple cycles of autocatalytic deposition (step 2). The average bi-layer shell thickness utilizing one or two autocatalytic cycles was 1.9 ± 0.3 μm and 4.66 ± 0.43 μm, respectively (see **Fig S1**). These values are based on 50 measurements conducted on 10 randomly selected particles from each batch.

XRD phase identification before and after the two-step CoP micro-encapsulation process is presented in Fig 1k and 1l, respectively. In the untreated state, hexagonal Zn phase (ICDD card No. 04-003-5661), Al-rich solid solution Al-0.48Zn phase (fcc, ICDD card No. 04-0207570), and native Al_2O_3 (ICDD card No. 00-056-0456) are all evident, as discussed in Ref. [26]. After the encapsulation process, a significant reduction in the intensities of diffraction peaks originating from the ZA–8 core indicates the presence of a shell layer. Additional reflections related to pure cubic Co (card No. 04-001-3273, $a = 2.5071$ Å) are evident in Fig 1l, in agreement with Fig 1j. The triclinic Doyleite phase, $Al(OH)_3$, was ascribed in Ref. [31] to the excess OH^- naturally present in the alkaline solution utilized in the autocatalytic deposition process.

During the healing process in SHMMC, the CoP shell encapsulating the ZA-8 particles serves an important mechanical function beyond acting as a diffusion barrier. First, the CoP shell should crack upon the propagation of the macro-crack through the Al 5083 matrix. This results in the exposure of the ZA–8 core and facilitates the capillary flow of ZA–8 melt out of the shell into the crack during the healing heat treatment. Second, following the healing process, some of the encapsulation remains partially filled with ZA–8, resulting in voids, likely weakening the MMC [3]. In this case, the micro-encapsulation should provide some structural integrity to compensate for the formation of the voids. To characterize the mechanical properties of the CoP-encapsulated ZA–8 particles, nanoindentation tests were performed.

Fig 2a,b shows the hardness and elastic modulus maps at the cross-section. In contrast, Fig 2c presents the corresponding *in situ* scanning probe microscope (SPM) topography analysis conducted on the same area following nanoindentation. A significant difference is evident between the hardness of the CoP shell (5.86 ± 0.56 GPa) and ZA–8 core (1.66 ± 0.31 GPa). However, the elastic modulus in both regions had similar values (82.36 ± 13.21 GPa and 81.56 ± 7.65 GPa for the shell and core, respectively). As the hardness of pure Co was previously reported as 3.14 GPa [34], we attribute the higher value measured here to the presence of P. It has been shown that the concentration of P in autocatalytically deposited CoP layers depends on the bath chemistry and deposition conditions [35]. Consequently, parameters such as the bath concentrations of cobalt sulfate ($CoSO_4$) and sodium hypophosphite (NaH_2PO_2), as well as solution pH, affect the microstructure, magnetic properties, elastic modulus, and microhardness of the CoP deposit [34,35].

The melting temperature of the LMPP was determined from DSC analysis of both untreated and micro-encapsulated ZA–8 LMPP (single or double micro-encapsulation cycles). All thermograms (**Fig S2**) exhibit a single endothermic peak at 382°C, corresponding to the absorbed latent heat associated with the melting of the LMPP.

Bright-field (BF) and dark-field (DF) imaging, electron diffraction, and EDS analyses from scanning/transmission electron microscopy (STEM) were employed to locally determine the phases and characterize the interfaces inside the core and between the core and the shell. The TEM sample was lifted out via a focused ion beam (FIB) from the region covering the Al 5083 matrix, Co coating, and ZnAl core materials. Aluminum has significant solubility in zinc, according to the Zn–Al phase diagram. The eutectoid alloy with duplex phase structure, which contains 77.7 wt% Zn is known for its superplastic behavior [36]. The eutectic alloy that contains 5 wt% Al and the dilute alloys (up to 1.1 wt% Al) can also show superplastic behavior.

Fig 3 shows selected results. STEM revealed several phases: large Al-rich phase zones, separated by Zn-rich phase zones within which a fine Al-rich phase co-existed. The interface between the CoP shell and the ZnAl core was found to be rich in oxygen in a non-uniform manner; Fig 3g,h,j reveals preferential depletion of Zn due to its selective dissolution. Stacking faults were observed in the CoP shell before SPS (not shown herein). Such defects are known to form relatively easily in hcp metals such as Co and to have great effect on the magnetic properties [37].

2.2. SPS fabrication and microstructural characterization of Al 5083–ZA-8/CoP MMC

Al 5083 and ZA–8 powder feedstocks were synthesized by gas atomization. Their chemical compositions, volume-weighted particle sizes, and sphericity factors are provided in **Table S1**. For more in-depth Al 5083 and ZA-8 powder feedstocks characterization, the reader is referred to [28,31].

SPS was used to process the Al 5083–ZA-8/CoP MMC (after two-cycle autocatalytic deposition of the CoP shell on the ZA-8 particles). The nature of densification and consolidation of the powder mixture during SPS was revealed by SPS data analysis. The variations in shrink rate and displacement could be related to the deformation of the LMPPs during SPS. The temperature of shrink start indicates the starting temperature for softening. The effects of different SPS parameter sets of consolidation pressure (20–100 MPa), temperature (350–400 °C), and holding time (3 min), on the density (as measured by Archimedes' principle), deformation of the ZnAl/CoP core/shell LMPPs, shell fracture, and leakage from them into the Al 5083 matrix (as observed by optical microscopy and SEM-EDS) were first studied. Less porosity (including triple-junction pores) was observed in MMCs sintered at high temperature and pressure. However, SPS at 400 °C increased the melting and leakage of Zn from the LMMPs into the matrix. Temperature holds of either 15 min or 3 × 3 min cycles helped decrease the porosity, but also resulted in an increased deformation of the large LMMPs and more significant leakage of Zn from the LMMPs into the Al 5083 matrix. In general, while maximal density was associated with the larger micro-encapsulated LMPPs, smaller LMPPs exhibited less plastic deformation, less cracking/fracture, and consequently less ZnAl melting and leakage into the Al matrix. In addition, it was observed that two cycles of CoP encapsulation for increased shell thickness resulted in an increase in the shrink start temperature, a reduction in the shrink rate, as well as in less cracking and fracture of the shell. The shrink start temperature was ~130 °C for large ZnAl particles (>75 μm), and ~150 °C for fine coated particles. Since smaller coated LMMPs exhibited less deformation and shell cracking and were more uniformly distributed in the MMC, their future use should be considered. Using smaller LMPPs also results in a higher volume fraction of Co, which should reduce vaporization during DED processing.

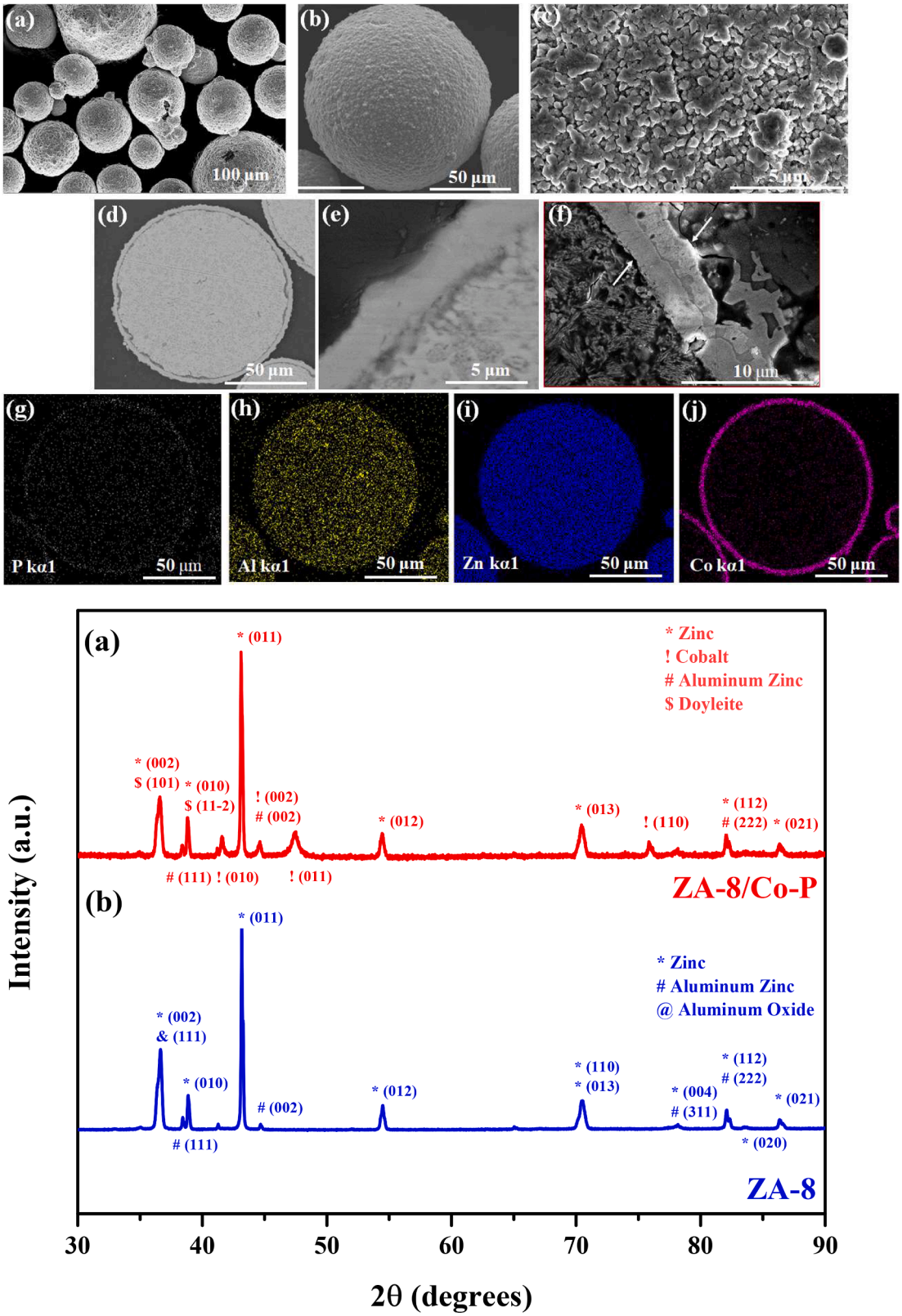

Fig 1. Autocatalytic deposition of CoP on ZA–8 low melting point particles (LMPPs) utilizing optimal conditions. (a) SEM secondary electron (SE) image revealing spherical particles with no agglomeration. (b) A zoomed-in image of (a). (c) SEM SE image revealing the surface morphology with micro-grooves. (d) SEM backscatter electron (BSE) image of a cross-section. (e) A zoomed-in image of (d) showing a continuous shell layer. (f) SEM BSE image reveals the two sublayers of the shell and the interface between them. (g–j) EDS elemental maps of P, Al, Zn, and Co, respectively. XRD patterns of: (k) Untreated ZA–8 LMPPs, (l) CoP-encapsulated ZA–8.

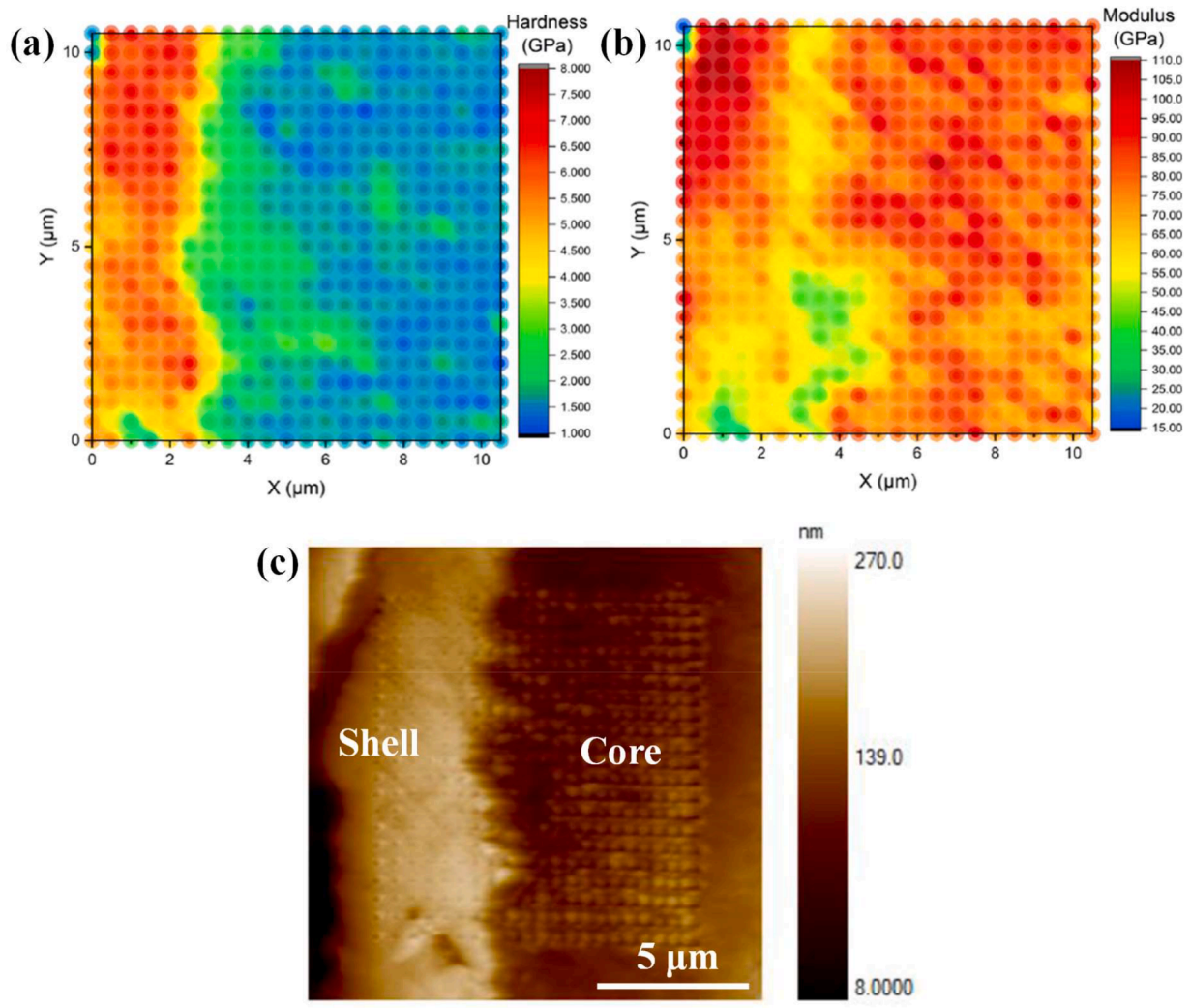

Fig 2. Nanoindentation analysis of CoP-micro-encapsulated ZA–8 low melting point particle (LMPP). (a) Hardness map. (b) Elastic modulus map. (c) In-situ scanning probe microscope (SPM) topography image of the analyzed area in (a,b).

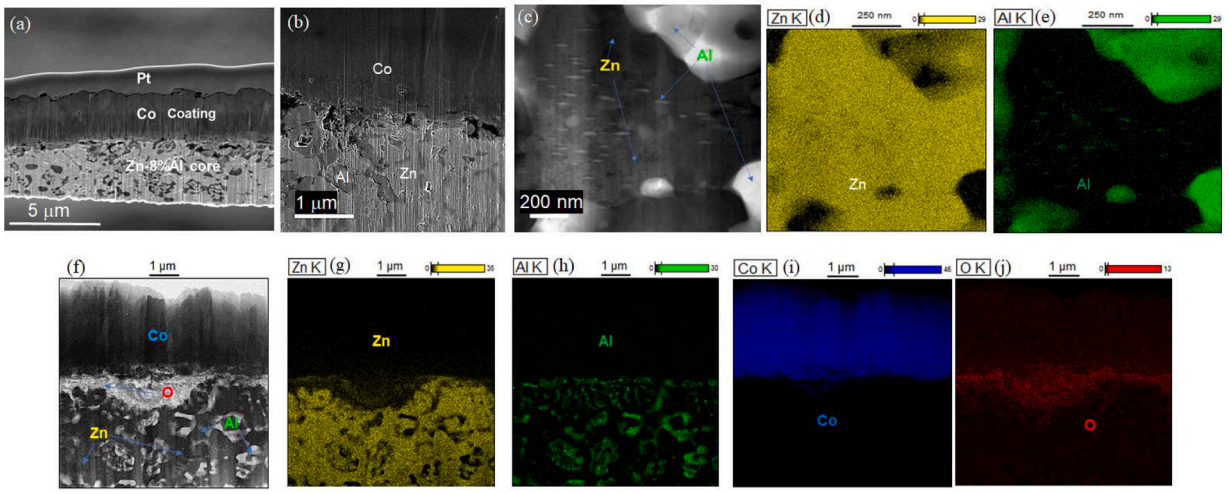

FIG 3. TEM imaging and elemental mapping of a core/shell ZnAl/Co particle before spark plasma sintering (SPS). (a) FIB'ed cross-section. (b) SEM mode showing Al- and Zn-rich phases in the core and the Co shell. (c) TEM BF image revealing coarse and fine Al-rich phase (bright) and Zn-rich phase (dark), (d,e) elemental mapping of Zn and Al in the core Zn–8Al core. (f) TEM BF image of the core/shell interface, (g–j) the related elemental mapping, revealing an oxygen-rich interface.

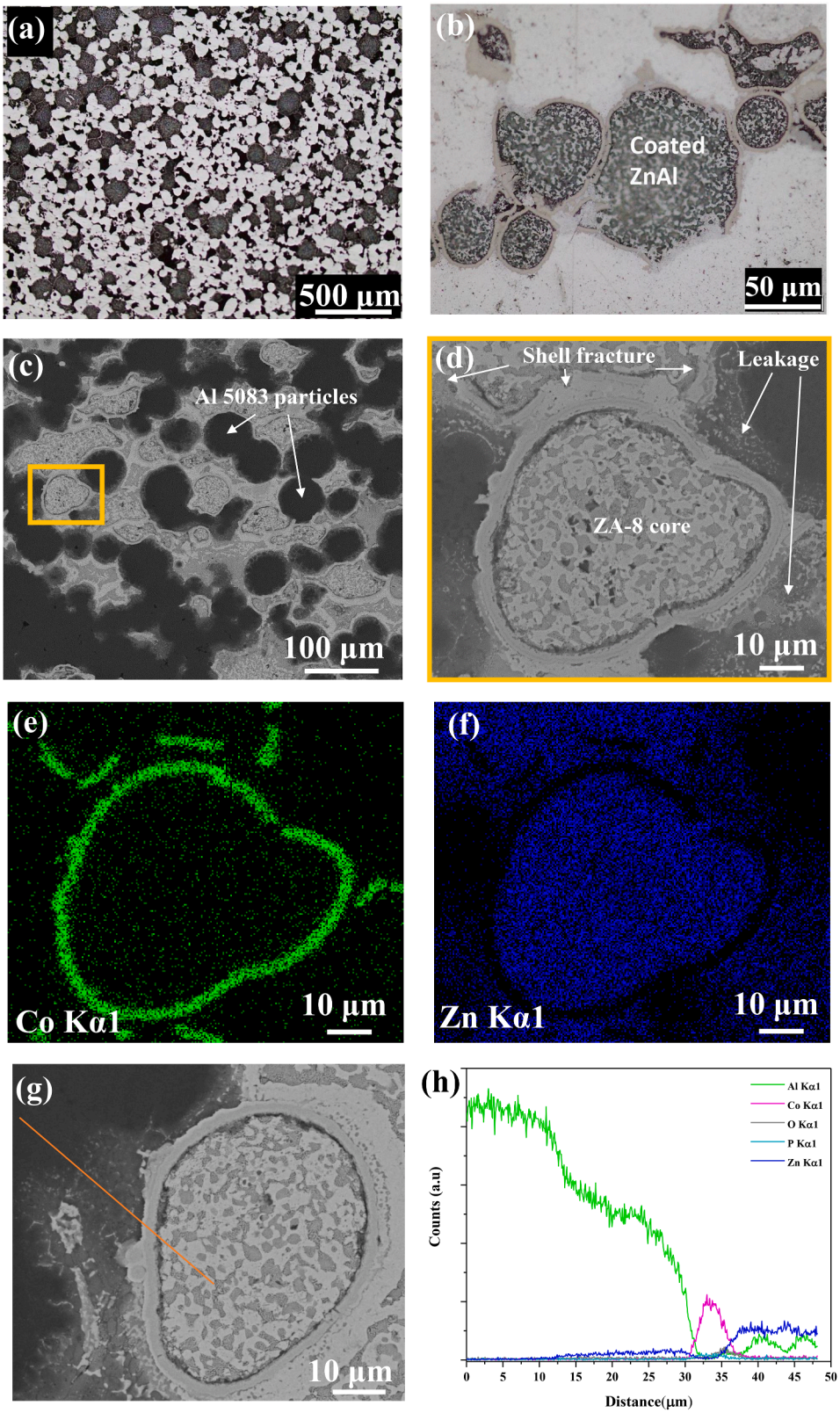

Fig 4. (a) Optical micrograph revealing a fairly dense SPS consolidated MMC consisted of Al-based (bright) and Zn-based (dark) particles. SPS conditions: 100 MPa, 350°C, and holding time of 3 min. (b) Optical micrograph highlighting the porosity (green arrow) and shell cracking (red arrows). (c) SEM image revealing the cross-section microstructure after the SPS consolidation of Al 5083 and the two-cycle micro-encapsulated ZA–8 LMPPs. (d) SEM higher magnification image of the orange rectangle zone in (c). (e,f) EDS elemental maps of Zn and Co corresponding to (d). (g) SEM image of a cross-section at a representative area. (h) EDS elemental line-scan analysis corresponding to (g).

Fig 4 reports optical microscopy and SEM/EDS characterization of the MMC sintered at 100 MPa, 350 °C, and holding time of 3 min. The process temperature was selected to be lower than the melting temperature of the ZA–8 LMPP to avoid as much as possible the formation of severe leakage and diffusion of the LMP material into the matrix during the SPS processing. The optical micrograph in Fig 4a shows a good dispersion of the micro-encapsulated LMPPs in the Al 5083 matrix and fairly high density after sintering. Optical micrographs at higher magnification (Fig 4b) reveal good metallurgical bonding between the CoP shell and the Al 5083 matrix but also some porosity and cracking of the shell. The inherent characteristics of SPS processing, in which compressive loads are applied during the consolidation process, result in partial fracture of the shell in some micro-encapsulated LMPPs (Fig 4a,d, e). As a result of the shell cracking, diffusion of the LMP material into the Al 5083 matrix occurs. Fig 4d–f shows SEM images and corresponding EDS maps of Co and Zn; shell cracking and leakage of the core alloy into the matrix are evident. Fig 4g,h shows a SEM image of the cross-section of a particle with the corresponding EDS elemental line scan analysis. The small micro-encapsulated particle in Fig 4g causes the deformation of a larger, conjugated micro-encapsulated LMPP in the background of the Al 5083 matrix. The line scan analysis shows a decrease in Al counts with a corresponding increase in Zn counts during the transition from the Al 5083 matrix to the leakage zone. As expected, an increase in Co and P counts is evident when reaching the shell, followed by an increase in Zn counts when reaching the ZA–8 core.

XRD analysis was utilized to determine the phase content of the SPS consolidated SHMMC (Fig 5). TOPAS Rietveld refinement revealed that before heat treatment, the material consisted of 63 wt% Al-rich solid-solution cubic phase $Al_{0.95}Zn_{0.05}$ (ICDD card No. 04-003-7050; a = 4.0690 Å), 21 wt% Al cubic phase (ICDD card No. 04-003-2966; a = 4.0473 Å), and 13 wt% Zn hcp phase (ICDD card No. 04-085-5877; a = 2.6683 Å, c = 4.9114 Å). In addition, 3 wt% $Mg(Zn,Co)_2$ hcp phase (ICDD card No. 04-005-1835; a = 5.2161 Å, c = 8.562 Å) was observed. This phase is ascribed to Zn leakage into the Al-Mg-based matrix. It should be noted that Co and Zn are very close in the periodic table. Thus, it is challenging to differentiate between the phases of these two elements. Consequently, the presence of Mg_2Zn intermetallic hcp phase (ICDD card No. 00-034-0457; a = 5.2161 Å, c = 8.562 Å) cannot be excluded.

Using FIB we prepared a TEM sample from a zone that contained Al 5083 matrix, CoP shell, and ZA–8 core (Fig 6a). A high density of dislocations observed in some Al 5083 grains (Fig 6b) is the consequence of plastic deformation during the SPS process. The ZnAl eutectic structure

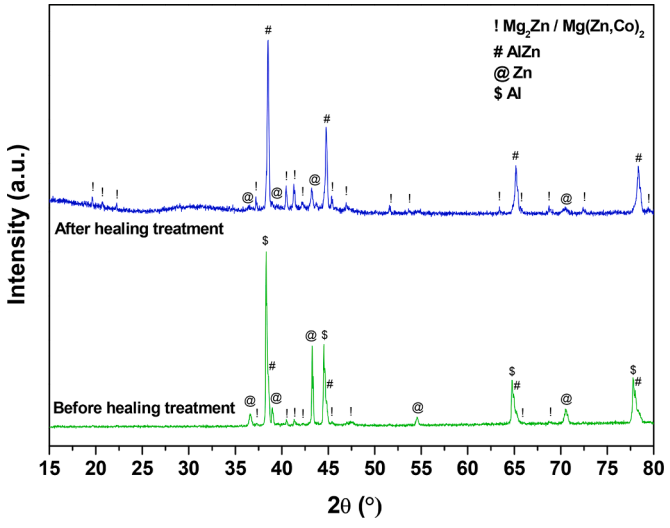

Fig 5. XRD patterns the SPS'ed SHMMC, before and after the thermal healing treatment.

observed in the ZnAl particles (Fig 6c) with its interlamellar spacing of 50–80 nm is different from that observed in the gas atomized ZnAl particles [30,31]; its formation indicates that the ZnAl particles were partially melted during SPS and subsequently re-solidified at a high cooling rate. Cracking of the shell was observed in some LMPPs (marked by red arrow in Fig 6d). EDS element maps in Fig 6d revealed that melted Zn diffused out of the cracked CoP shell. During the SPS process, Zn underwent reactions with elements in the CoP shell and the Al5083 matrix, forming precipitates with different compositions, morphologies and sizes (see Fig 6e-g). In Fig 6e (identified as region (i) in Fig 6d), eutectic lamellar structure, consisting of alternating Zn-Co-rich and Al-rich layers (40-100 nm in thickness), is observed near the cracked CoP shell. As seen in Fig 6f (marked as region (iii) in Fig 6d), coarse (200–500 nm) Mg-Zn-Co-rich precipitates are formed at grain boundaries in the Al 5083 matrix. Fig 6g (magnification of region (iii) in Fig 6f) reveals high density of fine (20–50 nm) Zn-(Co)-rich precipitates formed inside the grains.

3. Self-Healing Demonstration

3.1. Procedure and macroscopic observations

The self-healing procedure was conducted as described in the methods section and shown in Figs 7, 10, 11, and 12. First, using the tensile fixture assembly, the SHMMC sample was subjected to axial tensile loading (Fig 7a,b). The tensile loading resulted in brittle fracture near the fixture grip, and not at the sample's notch root (Fig 7c). Such a fracture indicates that the stress concentration formed next to the boundary conditions (fixture grip) is higher than that at the notch root, according to ASTM D3039 [38]. The sample fixture was then adjusted to the compression assembly mode and axially compressed at ~250 MPa, followed by fixture locking to retain the induced compression load during the healing treatment (Fig 7d,e). According to the Johnson-Cook model, the high compression stress of 250 MPa was selected to simulate the stress for crack closure by SMA [39]. This high stress did not cause diffusion bonding, as shown below.

Solid-state joining of Al and its alloys is considered a significant challenge, ascribed to a stable native aluminum oxide layer over the surface [40]. This native oxide layer serves as a diffusion barrier that impedes the metal-to-metal bonding and results in inferior metallurgical bonding [40]. Generally, it is advised to either fully or partially remove this oxide layer and apply surface cleaning before the joining process to achieve good interfacial bonding [41]. It is crucial to highlight that the current study did not involve any preliminary preparation of the fracture surface, such as mechanical grinding, surface cleaning, or chemical etching of the natural oxide layer. Instead, Mg vapor was used as a reducing agent to reduce the native aluminum oxide layer that had formed over the fractured surface, following the Ellingham diagram [42]. One can expect that during the thermal self-healing treatment at 420°C, the Mg vapor will have a pressure of ~0.01 Torr [43]. The Mg vapor is transported with the Ar flow to reduce the native oxide layer, as Mg has a lower Gibbs free energy of oxidation compared to Al. Reducing the oxide layer promotes more effective metallurgical bonding between the two fracture surfaces. It is important to note that self-healing experiments conducted without Mg vapor in the tube furnace resulted in lack of metallurgical bonding between the fracture surfaces to be joined. In contrast, when Mg vapor was introduced into the system, it enabled an effective metallurgical bonding, thus healing the fractured surfaces (Fig 7f).

3.2. The chemistry and microstructure of the healed MMC and the self-healing mechanism

Fig 8 shows SEM images acquired at the cross-section of the sample in Fig 7f. Fig 8a,b shows the healed sample at the macro-scale. Fig 8b is a higher magnification image of the white ellipse area in Fig 8a. The

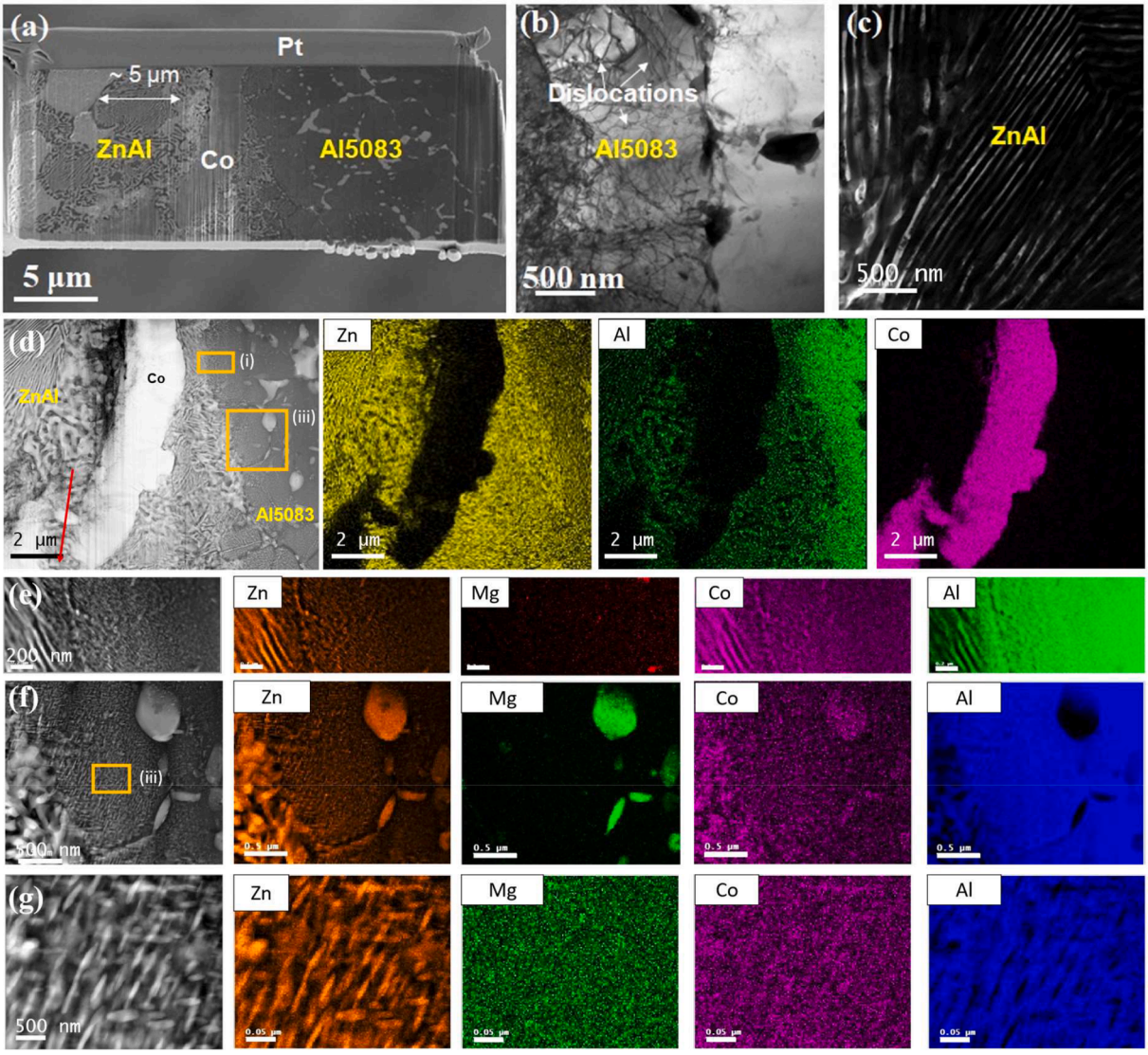

Fig 6. Electron microscopy and EDS characterization of the SPS consolidated SHMMC before thermal healing treatment. (a) SEM image of the FIB'ed specimen. (b) BF TEM image showing dislocations in the Al 5083 matrix. (c) BF TEM image of ZnAl eutectic lamellar structure within LMMP particles. (d) DF STEM image showing cracking of the CoP shell, and the corresponding STEM EDS elemental maps in region (i), showing diffusion of melted ZnAl from the core of the LMMP into the Al 5083 matrix. (e) STEM EDS maps from region (i) in (d), showing the formation of lamellar structure with alternating Zn-Co-rich and Al-rich layers in the Al 5083 matrix near the CoP shell. (f) STEM EDS maps from region (iii), showing coarse Mg-Zn-Co-rich phases formed at grain boundaries. (g) STEM EDS maps from region (iii) in (f), showing fine Zn-(Co) particles nucleated inside the grains. The scale bars in the element maps equal 2 µm (d), 0.2 µm (e), 0.5 µm (f), and 0.05 µm (g).

orange dashed rectangle in Fig 8b marks the fracture zone. An outstanding healing at the microscopic scale is evident. It is also evident that micro-encapsulated LMPPs were fractured, resulting in the fragmentation of the CoP shell and in the diffusion of the ZA–8 core material into the Al 5083 matrix, not only near the fracture surface but within the entire sample. The fracture is attributed to the applied compression loading methodology during self-healing, which involves the uniform compression of the SHMMC sample. This macroscopic applied loading differs from Svetlizky's self-healing concept (presented in Section 1), which relies on the SMA to contract the fractured surfaces and reduce the fracture volume locally. Fig 8c depicts the formed microstructure after the self-healing heat treatment. During heat treatment, the ZA–8 core material leaked out through the cracked CoP shell and diffused into the Al 5083 matrix during the self-healing heat treatment. Local EDS analysis at the four stars in Fig 8c reveals (Table 1) the formation of two main phases, a Zn-rich (bright) phase and an Al-rich (dark) phase. Interestingly, the Zn-rich phase contains Mg (see spectra 1 & 2), whereas the Al-rich phase does not (see spectra 3 & 4). The Al–Zn phase diagram [36] shows the high solubility of Zn in Al, while the Mg–Zn phase diagram shows the formation of Mg–Zn intermetallic compounds due to the preferential reaction of Zn with Mg [44]. The presence of elements such as Al, Zn, Mg, and Cu may indicate the formation of intermetallic compounds during the self-healing heat treatment. From Table 1, the segregation of Mg into the Zn-rich phase is evident. This is not surprising given the high thermodynamic affinity between Mg and Zn, as evident from their binary phase diagram. The origin of this Mg is most likely the Al 5083 matrix, and not the Mg vapor in the furnace (the Mg vapor pressure and time are insufficient for such Mg segregation).

Fig 8d shows a magnification of the area marked by a blue square in Fig 8b. Metallurgical bonding was not formed to heal the crack in areas where the Zn-rich phase was either absent or at low concentration. Fig 8e,f shows representative SEM images of the crack healing zone at two locations. The crack propagation morphology is distinct (some areas resemble "crack stitching"), and dashed green lines outline its propagation path. It is evident that along the crack propagation path, the Zn-rich phase acts as a filling agent that facilitates metallurgical bonding to

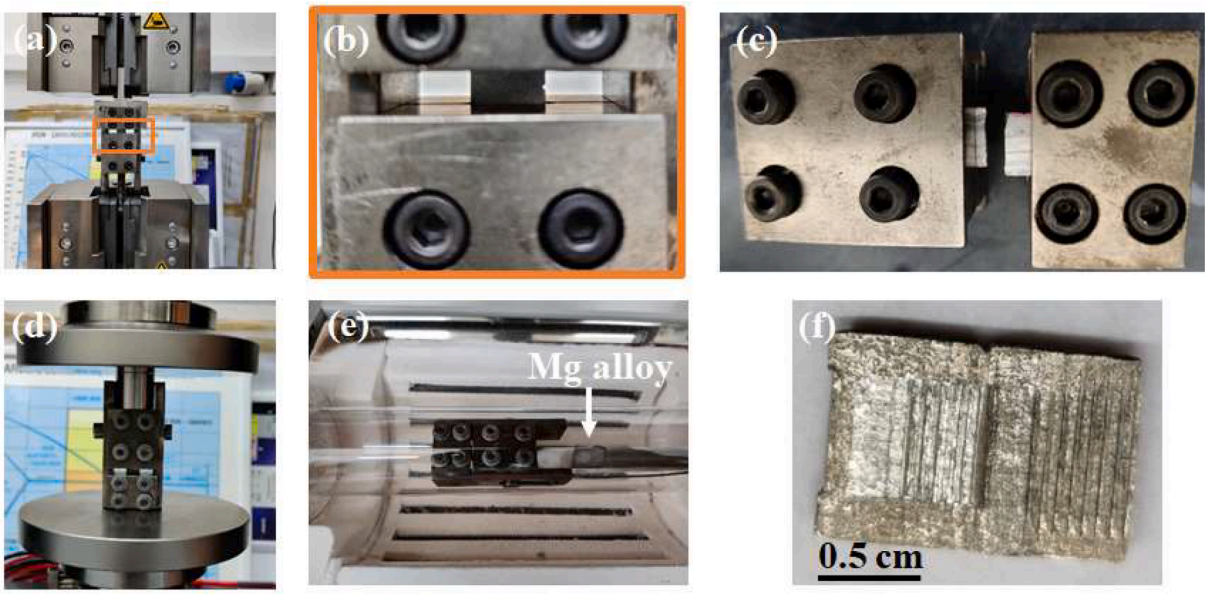

FIG 7. CCD camera images showing the experimental sequence. (a) Sample fixture in the tensile assembly mode. (b) Zoom-in of the orange rectangle zone in (a), showing sample fixation. (c) Sample brittle fracture after tensile loading. (d) Sample fixture in the compression assembly mode. (e) Sample fixture placed in the tube furnace for the self-healing heat treatment. (f) Healed SHMMC after the self-healing heat treatment of the fractured sample in (c).

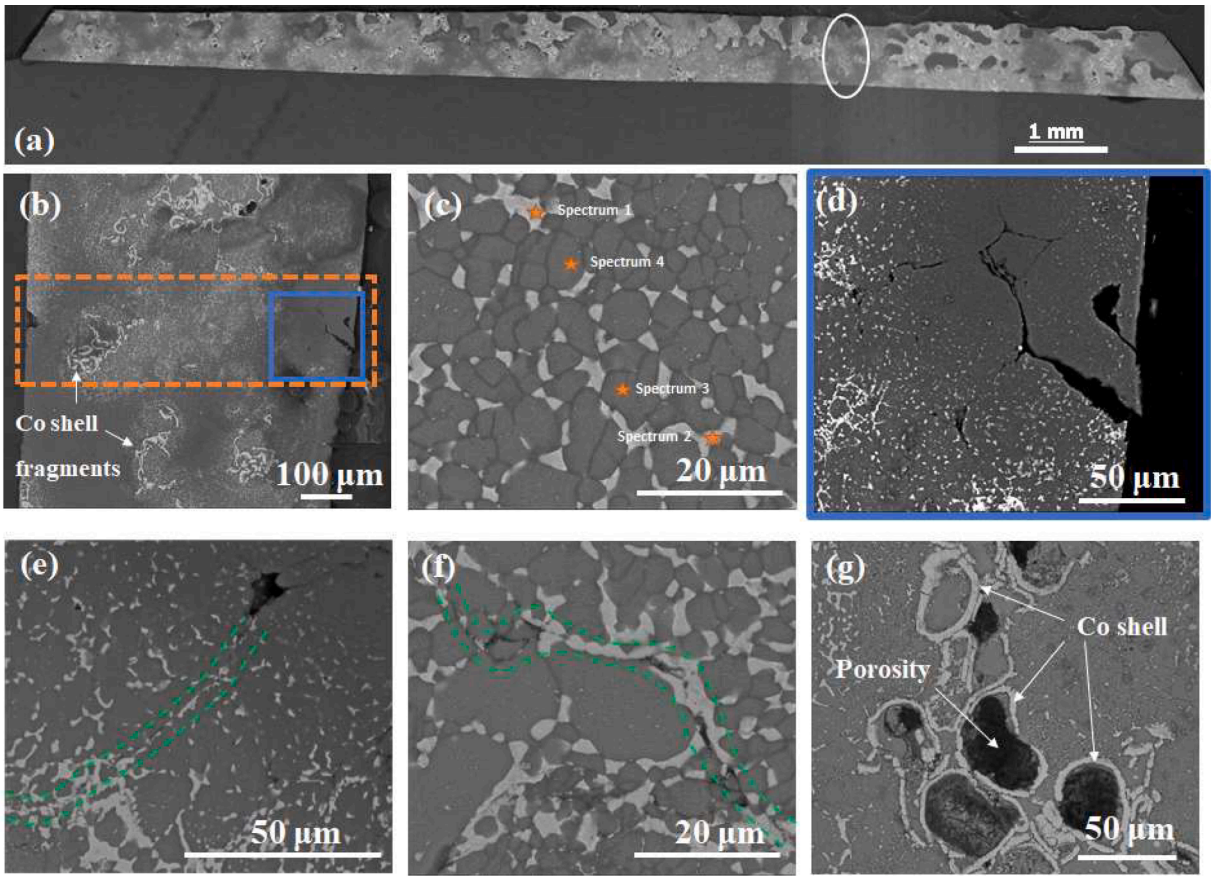

Fig 8. SEM images of the cross-section of the healed sample from Fig 7f. (a,b) Macroscopic view of the original fracture zone, demonstrating excellent healing. Fig 8b is a high magnification image of the white ellipse area in (a). (c) Formation of a Zn-rich phase (bright) and an Al-rich phase (dark). Orange stars mark the positions for local EDS analysis (Table 1). (d) High magnification image of the blue square zone in (b). (e,f) Representative images of the crack healing zone at two locations. (g) Porosity formation during self-healing heat treatment.

TABLE 1
EDS local chemical analysis (wt%) at the four points in the SHMMC cross-section marked by orange stars in Fig 8c.

Position	Zn	Al	Mg	Si	Cu	Co
Spectrum 1	64.33	19.04	11.03	3.47	1.55	0.58
Spectrum 2	64.89	17.24	13.15	2.95	1.02	0.74
Spectrum 3	29.09	69.42	-	1.49	-	-
Spectrum 4	31.50	67.60	-	0.90	-	-

heal the crack. Interestingly, at areas far from the crack propagation path, the Zn-rich phase precipitates along the grain boundaries of the Al-rich phase and exhibits a relatively equiaxed grain shape. In contrast, along the crack propagation path, the Zn-rich phase establishes a relatively continuous nucleation, facilitating transient liquid phase bonding (TLPB) between the two fracture surfaces to heal the fracture. The fact that full healing did not occur in Al-rich zones (darker areas in Fig 8b–d) further supports the conclusion that solid-state diffusion bonding [45] is not the mechanism of self-healing. Instead, TLPB [46–48] is suggested to be responsible for fracture healing.

Interfacial voids could have formed due to surface asperities when the two fracture surfaces were in contact. The variations in the width of the pre-crack are primarily attributed to the non-uniform plastic deformation of the rectangular samples during hot compression. Fig 8g shows the CoP shell morphology after the self-healing heat treatment. Unlike Zn, Co does not dissolve in the Al matrix. It should be noted that some of the CoP shells were partly damaged already during SPS processing (see Section 2.3). Yet, it seems that due to the uniform sample compression during the self-healing heat treatment, more damage was caused to the shells. Future utilization of AM technology to fabricate such SHMMCs that incorporate Al-based matrix, homogeneously distributed micro-encapsulated LMPPs, and continuous SMA fibers can potentially overcome this issue, as: 1) No external mechanical loading will be involved during fabrication, and 2) The mechanical crack contraction pressure of the SMA will be applied locally along the crack propagation path, thus

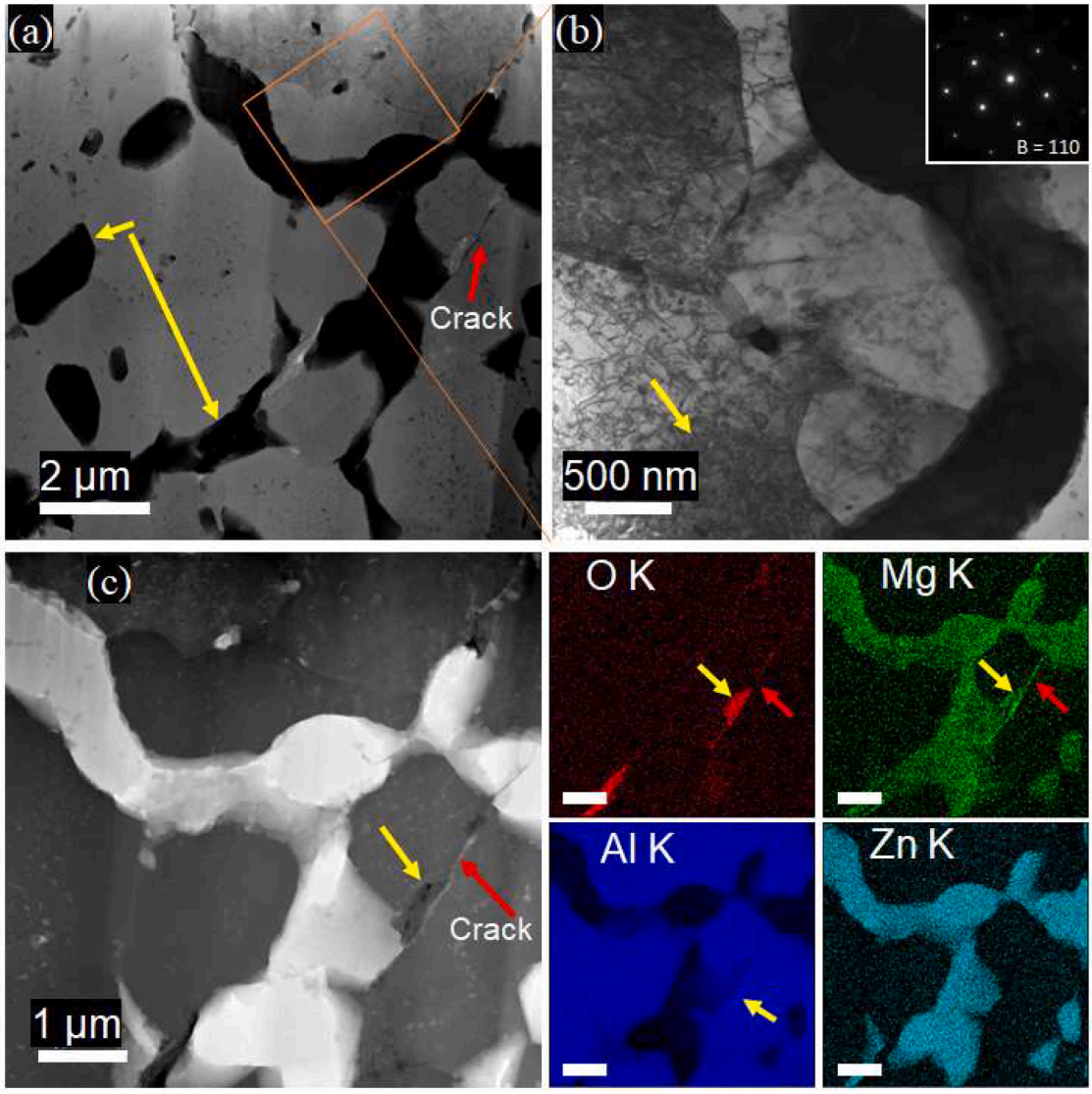

Fig 9. STEM characterization of the SPS consolidated SHMMC after thermal healing treatment. (a) BF STEM image revealing that Zn reacted with the Al matrix to form precipitates (marked by yellow arrows). A crack is marked by red arrow. (b) BF TEM high-magnification image of the orange rectangle in (a) showing dislocations in the Al grain, which probably formed during SPS. Inset in (b) is the selected area diffraction pattern for the Al alloy matrix along the <110> zone axis. A yellow arrow marks a region of high density of dislocations. (c) DF STEM image of a zone with a micro-crack (marked by red arrow) and the corresponding EDS elemental maps revealing precipitates that contain Zn and Mg (possibly, Mg_2Zn_{11}, white zones in the DF image). MgO and/or $MgAl_2O_4$ oxides (marked by yellow arrows), which either induced crack formation or formed along an existing crack during the self-healing process, are evident. All scale bars in the element maps equal 1 µm.

not affecting distant micro-encapsulated LMPPs. Fig 8g also shows the porosity formation during the self-healing heat treatment. This porosity is ascribed to the ZA–8 LMP filler leaking out through the CoP shell during the self-healing heat treatment.

XRD analysis (Fig 5) was utilized to determine the phase content before and after self-healing heat treatment of the SPS consolidated SHMMC. TOPAS Rietveld refinement revealed that after the self-healing heat treatment the material consisted of 80 wt% $Al_{0.9}Zn_{0.1}$ cubic phase (ICDD card No. 04-018-1292; a = 4.0438 Å), 14 wt% $Mg(Zn,Co)_2$ hcp phase (ICDD card No. 04-005-1835; a = 5.2133 Å, c = 8.557 Å), and 6 wt % Zn hcp phase (ICDD card No. 01-080-4436; a = 2.6660 Å, c = 4.925 Å). As mentioned before, the presence of hcp Mg_2Zn intermetallic phase (ICDD card No. 00-034-0457; a = 5.2161 Å, c = 8.562 Å) cannot be excluded.

Fig 9 shows the results of STEM characterization of the SHMMC produced through SPS after undergoing self-healing thermal treatment. The analysis reveals that Zn reacted with the Al 5083 matrix, forming precipitates (Fig 9a,c). Furthermore, Fig 9b displays a high density of dislocations in the Al grains, which may have arisen during SPS. Zn-Mg-rich precipitates, which may be Mg_2Zn_{11}, and MgO or $MgAl_2O_4$ oxides (Fig 9c) are found alongside the cracks, indicating that these phases either initiated crack formation or developed along an existing crack during the self-healing process. The latter possibility aligns with the TLPB mechanism.

4. Conclusions

A novel, generic metal matrix composites (MMCs) design with self-healing capability at the macro-scale was presented. As a proof of concept, spark plasma sintering (SPS) was used to fabricate an MMC consisting of an Al 5083 matrix and Zn–8Al low melting point particles (LMPPs). The latter were micro-encapsulated in a CoP thermal and diffusion barrier by a novel two-step electroless deposition process. Optimal SPS parameters were identified as a tradeoff between maximal density and minimal particle deformation, shell fracture, and ZnAl melting and leakage into the Al matrix. The ability to encapsulate individual powder particles in a dense and uniform material represents a new methodology of LMPP encapsulation for SHMMC applications. Despite some partial diffusion of the LMMP core into the Al 5083 matrix during consolidation (attributed to fracture of the CoP shell due to the high SPS pressure), we demonstrate full healing of a complete, cm-scale fracture. Subsequent heat treatment under extrinsic compression force (as an alternative to intrinsic SMA) and under magnesium vapor effectively healed a total fracture at the centimeter scale. High local Zn concentration was found to be essential for self-healing, enabling the formation of precipitates near the crack surfaces. Transient liquid phase bonding (TLPB) was identified as the healing mechanism.

5. Methods

Powder characterization. Two powder feedstocks were used: 1) Al 5083, 2) ZA–8. Both powder feedstocks were pre-alloyed and processed for this study by gas atomization by TLS Technik GmbH & Co. Spezialpulver KG (Bitterfeld-Wolfen, Germany). Inductively coupled plasma optical emission spectrometry (ICP-OES, PlasmaQuant PQ9000, Analytik Jena AG, Jena, Germany) was used to analyze the chemical composition of both powder feedstocks. For cross-section characterization, the powder was cold mounted in acrylic resin (Struers, Copenhagen, Denmark). Mechanical grinding was performed using 1200, 2500, and 4000 grit SiC grinding papers, followed by mechanical polishing using 1 μm diamond suspension. Morphological analysis was conducted by a SEM (Quanta 200 FEG, FEI, Waltham, MA, USA) equipped with EDS (INCA detector, Oxford Instruments, Abington, UK). The PSD of both powders was measured by a QICPIC dynamic image analysis system (Sympatec GmbH, Clausthal-Zellerfeld, Germany). XRD measurements were conducted using a D8 ADVANCE diffractometer (Bruker AXS, Madison, WI, USA) and Cu-Kα radiation source. TOPAS software, ver. 5 (Bruker AXS, Madison, WI, USA), was utilized for phase identification analysis using the Rietveld refinement technique (R_{wp} = 8.311). DSC (Q20, TA Instruments, New Castle, DE, USA) was used to determine the effect of CoP micro-encapsulation on the melting temperature of the ZA–8 LMPP. DSC measurements were run using alumina crucibles, nitrogen atmosphere, and heating/cooling rates of 2°C min^{-1}. Nano-indentation tests were conducted using Hysitron TS77 Select Nano-Indenter (Bruker, Billerica, MA, USA), to evaluate the hardness and the elastic modulus of the ZA–8/CoP core/shell powder. Testing was done using a diamond Berkovich probe calibrated on a fused quartz sample. The core/shell cross-section was analyzed using a mapping 22 × 22 indentation matrix with separation of 500 nm between indentations at a peak load of 200 μN. The Oliver & Pharr method [49] was utilized to analyze each indentation's hardness and elastic modulus.

Two-step core-shell micro-encapsulation process. The LMPP core/shell micro-encapsulation process was conducted according to the methodology developed by Svetlizky et al [31]. The suspension solution was vigorously stirred throughout both deposition steps, using mechanical stirring, to allow uniform deposition on individual ZA–8 LMPPs and to avoid agglomeration. Each solution was kept in a temperature-controlled bath. The ZA–8 LMPPs were gradually introduced into the solution to avoid possible aggregation. The micro-encapsulated LMPPs were rinsed using ethanol absolute after each deposition step, to remove any residual solution, and were then dried at 70°C in atmospheric conditions. The Co cementation process conditions and the chemical composition of the electrolyte solution were selected based on an optimization process (unpublished data), in which the effects of process duration, temperature, and cobalt chloride concentration on the primary Co layer were investigated. The electrolyte solution was prepared by dissolving 0.1 M $CoCl_2{\cdot}6H_2O$ in ethanol absolute. The electrolyte solution was heated to 65–70°C prior to the gradual introduction of the ZA–8 LMPPs, and was mechanically stirred for 15 min. A second shell layer of CoP was deposited using an autocatalytic deposition process. The process conditions and electrolyte solution composition used herein (see Table 2) are the outcome of an optimization process (unpublished data). Glycine amino acid was used as a stabilizing agent, Boric acid was used as a buffer, and sodium hypophosphite was used as a reducing agent. Transmission electron microscopy (TEM) specimens of CoP-encapsulated ZA–8 LMPPs were prepared by focused ion beam (FIB) using a FEI Quanta 3D FEG dual-beam FIB-SEM with a gallium ion beam. The microstructure of CoP-encapsulated ZA–8 LMPP was analyzed using a JEOL JEM-2800 Schottky field-emission scanning/transmission electron microscope (FE-STEM) operated at an accelerating voltage of 200 kV, attached with a Gatan OneView IS camera and dual dry solid-state 100 mm^2 energy-dispersive X-ray spectroscopy (EDS) detectors.

Processing of the SHMMC by SPS. SPS was preferred in this study over stir casting and AM for the processing of the SHMMC. SPS utilizes a combination of uniaxial mechanical pressure-induced sintering with pulsed current. The pressure enables plastic flow of the consolidated material, while the current that passes through the graphite die and the powder (if conductive) heats the powder internally and enables an

Table 2
Optimized electrolyte composition and process conditions for autocatalytic deposition of CoP.

Electrolyte composition and process conditions	Specification
$CoSO_4{\cdot}6H_2O$	0.10 M
NaH_2PO_2	0.50 M
Glycine	0.40 M
Boric acid	0.30 M
pH	10
Time	30–40 min
Temperature	65–70°C
Solvent	Deionized water

electrical field diffusion effect. The main advantages of SPS processing include reduced sintering temperature (200–300 °C lower than in conventional sintering), rapid sintering which restrains grain growth, and precision control of heat, cooling, and pressure, resulting in a fully dense sample after sintering [50,51]. In the current work, the powder mixture comprised 80 vol% Al 5083 powder feedstock and 20 vol% ZA–8/CoP micro-encapsulated LMPPs (after two-cycle autocatalytic deposition). The two powders were mixed together for 1 h using a V-blender. SPS system (Dr. Sinter SPS-825S, SPS Syntex Inc., Japan) was utilized to consolidate the powder mixture into bulk samples. A graphite die with 19 mm inner diameter and 76 mm height was used to fabricate composite cylinders with the obtained size of 19 mm diameter and 15 mm in height. The process temperature was monitored using a K-type thermocouple. SPS processing data analysis revealed the nature of densification and consolidation of the powder mixture during SPS. The effects of different SPS parameter sets of consolidation pressure (20–100 MPa), temperature (350–400 °C), and holding time (3, 5, or 3 × 3 min) on the density (as measured by the Archimedes' principle), deformation of the ZnAl/CoP core/shell LMPPs, shell fracture, and leakage from them into the Al 5083 matrix (as observed by optical microscopy and SEM-EDS) were first studied. Finally, the SPS process sequence consisted of four steps: (1) initial heating of the powder mixture to 330°C while applying pressure of ~33 MPa for 3 min, (2) temperature increase to 350 °C with gradual increase of pressure to 100 MPa for 1 min, (3) pressure and temperature holding for 3 min, (4) pressure turn off, and temperature allowed to reduce to room temperature after which sample was extracted from of the die.

Self-healing demonstration. Using a wet abrasive cut-off machine, the MMC samples produced through SPS were sectioned, with their final dimensions outlined in Fig 10. A notch measuring 45°, $r = 0.1$ mm, $L = 0.3$ mm was introduced. These samples were intended to be used with a custom-made tension/compression sample fixture that was specifically created for this study (Figs 11 & 12). The design of this fixture was motivated by the necessity to fracture/crack the sample, unite the fractured surfaces with an optimal fit while maintaining a pre-defined retained compressive load, and position the fixture assembly inside a tube furnace to facilitate the healing process. Furthermore, the sample fixture was designed to prevent potential buckling and slip of the sample during the tensile/compressive loading.

The designed sample fixture has two assembly modes: 1) tensile mode (Fig 10) to facilitate the crack/fracture, and 2) compressive mode (Fig 11) to facilitate compressive loading with the ability to retain pressure in the tube furnace during the healing treatment. Fig 6 demonstrates the experimental sequence. First, the sample was placed in the fixture using the tensile assembly mode. Utilizing a Zwick/Roell Z050 testing machine equipped with a 50 kN load cell, axial loading was applied until failure. Second, the fixture was adjusted to a compressive assembly mode. The compressive assembly mode accommodates the alignment of the two fractured surfaces with an optimal match by allowing only axial movement of one side of the fractured sample along with guides. Using the Zwick/Roell Z050 testing machine in compression mode, the fractured surfaces were compressed to a final load of 250 MPa, followed by fixture locking to retain the induced compressive load during the healing treatment. Finally, the sample fixture was placed in a tube furnace for the healing treatment at 420 °C for 1 h under an argon environment. First, the tube cell was purged with argon applying 1 L min^{-1} for 1 h at room temperature, followed by modifying the argon flow rate to 0.3 L min^{-1}. A small piece of Mg alloy (AZ31) was placed next to the sample fixture (upstream with the argon flow) during the healing treatment to facilitate the reduction of the aluminum oxide layer using the Mg vapor generated during the heat treatment. The healing treatment temperature was monitored using a type-K thermocouple, placed next to the sample inside the tube furnace. The system was allowed to cool down to room temperature under an argon environment prior to fixture disassembly. For metallurgical characterization, the healed samples were cold mounted in acrylic resin (Struers, Copenhagen, Denmark) and mechanically ground on 600, 800, 1200, 2500, and 4000 grit SiC grinding papers. Final mechanical polishing was done using 1 μm diamond suspension followed by 0.1 μm silica suspension. The self-healed samples were characterized using a variety of analytical techniques. SEM-EDS was used to characterize the crack propagation route, microstructure, and chemistry at the cross-section. A Quanta 200 FEG SEM (FEI, Waltham, MA, USA) was operated at 20 keV and high vacuum. The attached EDS INCA detector (Oxford Instruments, Abington, UK) was used for local chemical analysis and elemental mapping. FEI Magellan 400 XHR SEM (Hillsboro, OR, USA) with EDS (Oxford Detector with AZtec Software) was also used for the microstructure and local chemical analysis. XRD (D8 ADVANCE, Bruker AXS, Madison, WI, USA) equipped with a Cu-Kα radiation source was used to determine the phase composition. The diffraction peak positions were identified using the International Committee for Diffraction Data (ICDD), and the crystallographic characteristics were analyzed using TOPAS software ver. 5

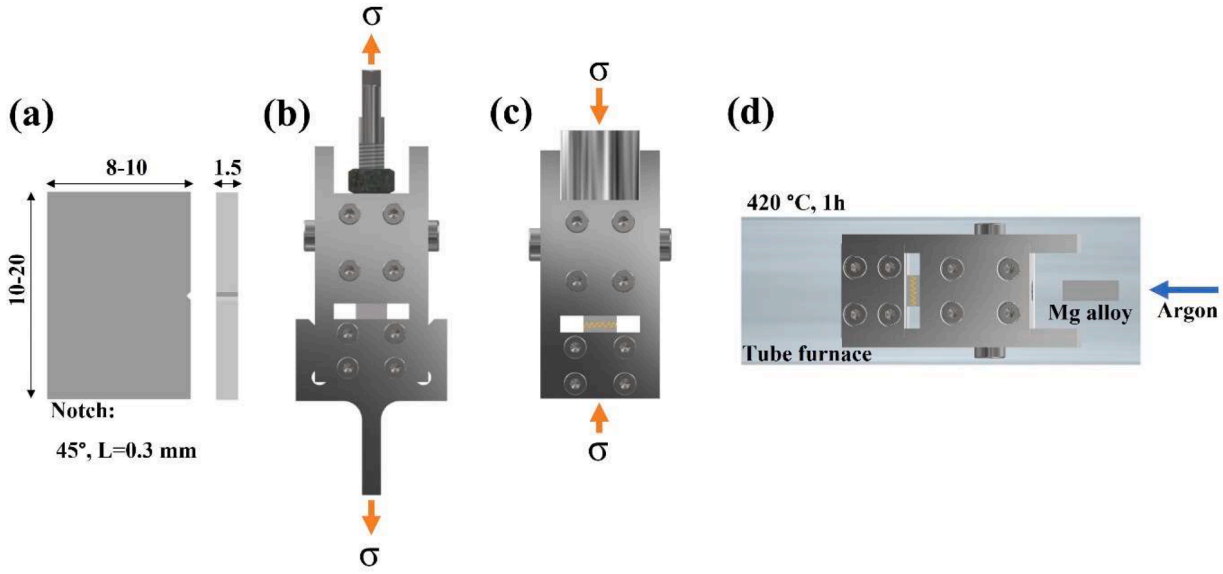

Fig 10. Sample dimensions and self-healing experimental methodology. (a) Sample dimensions. (b) Sample fixture in the tensile assembly mode. (c) Sample fixture in the compression assembly mode. (d) Self-healing heat treatment schematic illustration. All dimensions are in mm.

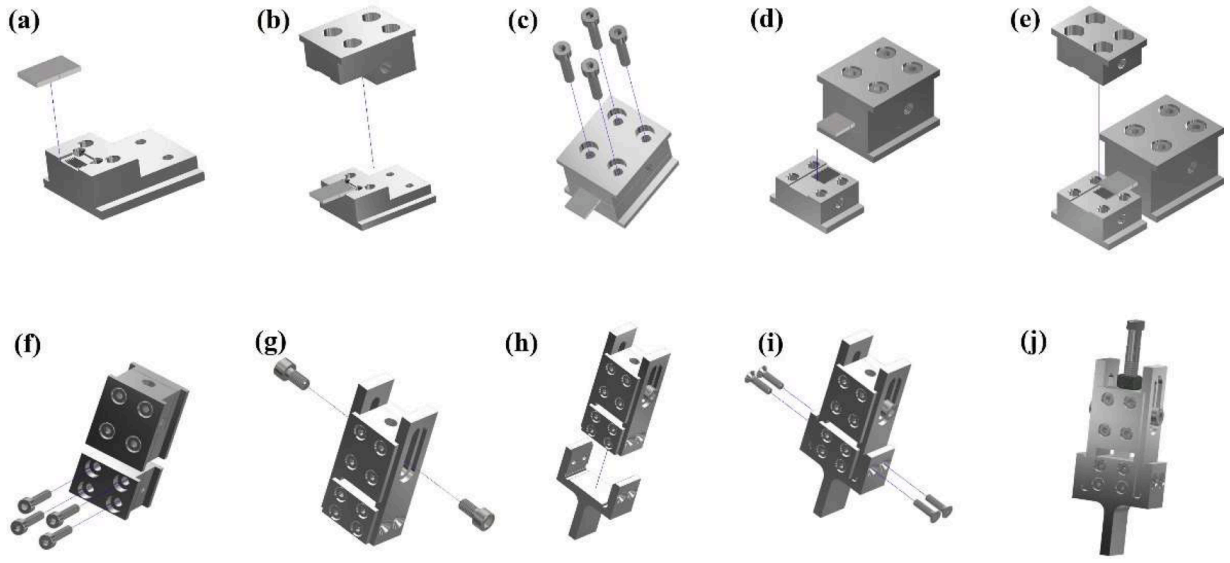

Fig 11. Assembly sequence illustration of the designed sample fixture in the tensile mode.

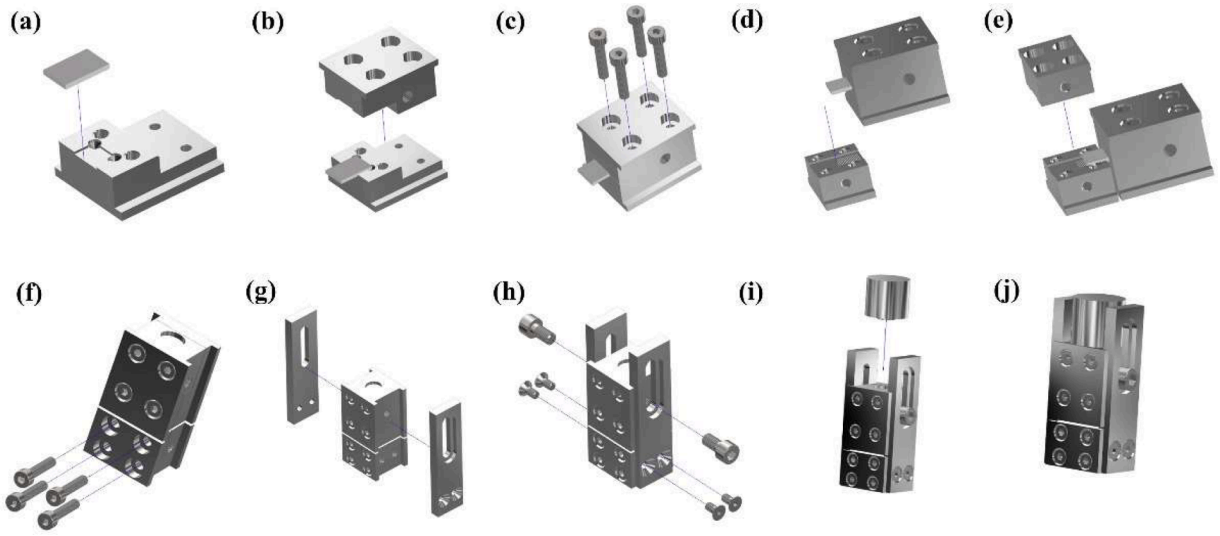

Fig 12. Assembly sequence illustration of the designed sample fixture in the compression mode.

(Bruker AXS, Madison, WI, USA) and Rietveld refinement. TEM specimens of SHMMCs before and after thermal self-healing treatment were prepared from regions of interest by FIB lift-out using a FEI Quanta 3D FEG dual-beam FIB-SEM. The microstructure, phase state, and elemental distribution in the TEM specimens were again analyzed using a JEOL JEM-2800 Schottky FE-STEM operated at an accelerating voltage of 200 kV, attached with a Gatan OneView IS camera and dual dry solid-state 100 mm^2 EDS detectors.

CRediT authorship contribution statement

David Svetlizky: Conceptualization, Data curation, Formal analysis, Investigation, Methodology, Visualization, Writing – original draft. **Baolong Zheng:** Investigation, Writing – review & editing. **Xin Wang:** Investigation, Writing – review & editing. **Sen Jiang:** Investigation, Writing – review & editing. **Lorenzo Valdevit:** Methodology, Writing – review & editing. **Julie M. Schoenung:** Conceptualization, Funding acquisition, Methodology, Project administration, Resources, Supervision, Writing – review & editing. **Enrique J. Lavernia:** Conceptualization, Funding acquisition, Methodology, Project administration, Resources, Supervision, Writing – review & editing. **Noam Eliaz:** Conceptualization, Formal analysis, Funding acquisition, Methodology, Project administration, Resources, Supervision, Visualization, Writing – review & editing.

Declaration of competing interest

The authors declare that they have no known competing financial interests or personal relationships that could have appeared to influence the work reported in this paper.

Data Availability

Data will be made available on request.

Acknowledgements

BZ, XW, SJ, LV, JMS, and EJL wish to acknowledge financial support from the Israel Ministry of Defense under P.O. Numbers 4440873734

and 4440783376. DS and NE gratefully acknowledge the financial support from the Israel Ministry of Defense (grant No. 4440783376). DS and NE thank Ariel Sharoni and Bar Ovadia for their assistance with the micro-encapsulation process, David Harel for his assistance in designing the sample fixture, and Eliran Hamo from the Department of Materials Science and Engineering and Olga Shamis from the School of Chemistry at Tel-Aviv University for their technical assistance with XRD and DSC measurements, respectively.

Supplementary materials

Supplementary material associated with this article can be found, in the online version, at doi:10.1016/j.apmt.2024.102148.

References

[1] M.V Manuel, in: Self-healing Mater. Fundam. Des. Strateg. Appl., Wiley-VCH, Chichester, 2009.
[2] N. K. Gupta, G. D. Thakre, M. Kumar, (Eds.: Shanker, K.; Shankar, R.; Sindhwani, R.), Springer Singapore, Singapore, 2019, pp. 543–550.
[3] B. Grabowski, C. C. Tasan, (Eds.: Hager, M. D.; Zwaag, S. van der; Schubert, U. S.), Springer International Publishing, Cham, 2016, pp. 387–407.
[4] K.K. Alaneme, M.O. Bodunrin, Appl. Mater. Today 6 (2017) 9.
[5] M. Nosonovsky, P.K. Rohatgi, Biomimetics in materials science: self-healing, self-lubricating, and self-cleaning materials, 152, Springer Science & Business Media, 2011.
[6] S.R. White, N.R. Sottos, P.H. Geubelle, J.S. Moore, M.R. Kessler, S.R. Sriram, E. N. Brown, Nature 409 (2001) 794.
[7] J. Martinez Lucci, R.S. Amano, P. Rohatgi, B. Schultz, in: Proc. ASME 2008 Int. Mechanical Eng. Congress and Exposition, ASME, Boston, 2008, pp. 1759–1768. October 31–November 6.
[8] K.K. Alaneme, O.I. Omosule, J. Miner, Mater. Charact. Eng. 3 (2014) 1.
[9] V. Srivastava, M. Gupta, J. Intell. Mater. Syst. Struct. 31 (2020) 2101.
[10] A.C. Ruzek, Master Thesis, University of Wisconsin-Milwaukee, 2009.
[11] M. C. Wright, M. Manuel, T. Wallace, "Fatigue resistance of liquid-assisted self-repairing aluminum alloys reinforced with shape memory alloys," NASA Technical Report NASA/TM-2013-216629, September 2013, can be found under https://ntrs.nasa.gov/api/citations/20140013299/downloads/20140013299.pdf (accessed: April 2023).
[12] "Self-healing aluminum metal matrix composite (MMC)," NASA report KSC-TOPS-80, can be found under https://technology.nasa.gov/patent/KSC-TOPS-80 (accessed: April 2023).
[13] M. V. Manuel, PhD Dissertation, Northwestern University 2007.
[14] B.S. Files, PhD Dissertation, Northwestern University, 1997.
[15] B.S. Files, G.B. Olson, in: Proceedings of the 2nd International Conference on Shape Memory & Superelastic Technologies, 1997.
[16] M.C. Wright, M. Manuel, T. Wallace, Thermo-mechanical evaluation of selfhealing metallic structures for aerospace vehicles utilizing shape memory alloys, in: NASA Aeronautics Mission Directorate FY11 Seedling Phase 1 Technical Seminar, 2013.
[17] M.V Manuel, G.B. Olson, Biomimetic self-healing metals, in: Proc. 1st Intl. Conf. Self-Healing Materials, 2007.
[18] C.R. Fisher, H.B. Henderson, M.S. Kesler, P. Zhu, G.E. Bean, M.C. Wright, J. A. Newman, L.C. Brinson, O. Figueroa, M.V. Manuel, Appl. Mater. Today 13 (2018) 64.
[19] M. C. Wright, M. Manuel, T. Wallace, A. Newman, C. Brinson, "Self-repairing fatigue damage in metallic structures for aerospace vehicles using shape memory alloy self-healing (SMASH) technology," NASA Report KSC-E-DAA-TN21605, March 2015, can be found under https://ntrs.nasa.gov/search.jsp?R=20150005789 (accessed: April 2023).
[20] J.B. Ferguson, B.F. Schultz, P.K. Rohatgi, Mater. Sci. Eng. A 620 (2015) 85.
[21] M.A. Poormir, S.M.R. Khalili, R. Eslami-Farsani, J. Intell. Mater. Syst. Struct. 29 (2018) 3972.
[22] C.R. Fisher, H.B. Henderson, M.S. Kesler, P. Zhu, G.E. Bean, M.C. Wright, J. A. Newman, L.C. Brinson, O. Figueroa III, M.V Manuel, Repairing large cracks and reversing fatigue damage in structural metals, Appl. Mater. Today 13 (2018) 64–68.
[23] D. Svetlizky, PhD Dissertation, Tel Aviv University, 2022.
[24] D. Svetlizky, M. Das, B. Zheng, A.L. Vyatskikh, S. Bose, A. Bandyopadhyay, J. M. Schoenung, E.J. Lavernia, N. Eliaz, Mater. Today 49 (2021) 271.
[25] A. Bandyopadhyay, K.D. Traxel, M. Lang, M. Juhasz, N. Eliaz, S. Bose, Mater. Today 52 (2022) 207.
[26] D. Svetlizky, B. Zheng, A. Vyatskikh, M. Das, S. Bose, A. Bandyopadhyay, J. M. Schoenung, E.J. Lavernia, N. Eliaz, Mater. Sci. Eng. A 840 (2022) 142967.
[27] N. Eliaz, D. Svetlizky, J. Schoenung, E. Lavernia, Y. Zhou, B. Zheng, International patent application PCT/US2020/065373, filed December 16, 2020.
[28] D. Svetlizky, B. Zheng, T. Buta, Y. Zhou, O. Golan, U. Breiman, R. Haj-Ali, J. M. Schoenung, E.J. Lavernia, N. Eliaz, Mater. Des. 192 (2020) 108763.
[29] D. Svetlizky, B. Zheng, D.M. Steinberg, J.M. Schoenung, E.J. Lavernia, N. Eliaz, J. Mater. Res. Technol. – JMR&T 17 (2022) 3157.
[30] D. Svetlizky, N. Eliaz, Coatings 11 (2021) 1389.
[31] D. Svetlizky, H. Kazimierczak, B. Ovadia, A. Sharoni, N. Eliaz, Materials 14 (2021) 834.
[32] R.C. Alkire, D.M. Kolb, E.J.O. Sullivan, Fundamental and practical aspects of the electroless deposition reaction. Advances, Electrochemical Science and Engineering, 2001.
[33] A.J. Bard, R. Parsons, J. Jordan, Standard potentials in aqueous solution, International Union of Pure and Applied Chemistry, New York, NY, 1985.
[34] A. Brenner, D.E. Couch, E.K. Williams, J. Res. Nat. Bur. Stand 44 (1950) 109.
[35] S. Cherneva, M. Stoycheva, R. Iankov, D. Stoychev, Int. Virtual J. For Sci., Techn. Innovat. Industry 8 (2011) 41.
[36] A. Pola, M. Tocci, F.E. Goodwin, Metals 10 (2020) 253.
[37] Y. Wang, Z. Yang, Q. Wu, W. Liu, Y. Li, H. Zhang, X. Ma, L. Cong, H. Wang, D. Zhang, Q. Lu, M. Yue, Mater. Charact. 187 (2022) 111861.
[38] ASTM D3039/D3039M –08, Standard test method for tensile properties of polymer matrix composite materials, ASTM International, West Conshohocken, PA, USA, 2008, p. 14.
[39] A. Shokry, S. Gowid, H. Mulki, G. Kharmanda, Materials (2023) 1574.
[40] A. Sunwoo, Scr. Metall. Mater. 31 (1994) 407.
[41] F. Wu, W. Zhou, Y. Han, X. Fu, Y. Xu, H. Hou, Materials 11 (2018) 1446.
[42] P. Stratton, Int. Heat Treat. Surf. Eng. 7 (2013) 70.
[43] C.B. Alcock, V.P. Itkin, M.K. Horrigan, Can. Metall. Q. 23 (1984) 309.
[44] A. Abdollahzadeh, A. Shokuhfar, J.M. Cabrera, A.P. Zhilyaev, H. Omidvar, J. Manuf. Process. 34 (2018) 18.
[45] H.S. Lee, Welding and joining of aerospace materials, 2nd edn., Elsevier, 2020 (Ed: M. Chaturvedi)Ch. 10.
[46] D.J. Fisher, Transient liquid phase bonding (2019).
[47] G.O. Cook III, C.D. Sorensen, J. Mater. Sci. 46 (2011) 5305.
[48] H. Chen, T. Hu, M. Li, Z. Zhao, IEEE Trans. Power Electronics 32 (2017) 441.
[49] W.C. Oliver, G.M. Pharr, J. Mater. Res. 7 (1992) 1564.
[50] Z.A. Munir, U. Anselmi-Tamburini, M. Ohyanagi, J. Mater. Sci. 41 (2006) 763.
[51] N. Saheb, Z. Iqbal, A. Khalil, A.S. Hakeem, N. Al Aqeeli, T. Laoui, A. Al-Qutub, R. Kirchner, J. Nanomaterials (2012) 2012. Article ID 983470.